

## Modeling hydration-mediated ion-ion interactions in electrolytes through oscillating Yukawa potentials

John Spaight, Rachel Downing , and Sylvio May 

*Department of Physics, North Dakota State University, Fargo, North Dakota 58108, USA*

Sidney J. de Carvalho  and Guilherme Volpe Bossa 

*Department of Physics, Institute of Biosciences, Humanities and Exact Sciences, São Paulo State University, São José do Rio Preto, São Paulo 15054-000, Brazil*



(Received 18 December 2019; revised manuscript received 6 March 2020; accepted 7 April 2020; published 8 May 2020)

Classical Poisson-Boltzmann theory represents a mean-field description of the electric double layer in the presence of only Coulomb interactions. However, aqueous solvents hydrate ions, which gives rise to additional hydration-mediated ion-ion interactions. Experimental and computational studies suggest damped oscillations to be a characteristic feature of these hydration-mediated interactions. We have therefore incorporated oscillating Yukawa potentials into the mean-field description of the electric double layer. This is accomplished by allowing the decay length of the Yukawa potential to be complex valued. Ion specificity emerges from assigning individual strengths and phases to the Yukawa potential for anion-anion, anion-cation, and cation-cation pairs as well as for anions and cations interacting with an electrode or macroion. Excluded volume interactions between ions are approximated by replacing the ideal gas entropy by that of a lattice gas. We derive mean-field equations for the Coulomb and Yukawa potentials and use their solutions to compute the differential capacitance for an isolated planar electrode and the pressure that acts between two planar, like-charged macroion surfaces. Attractive interactions appear if the surface charge density of the macroions is sufficiently small.

DOI: [10.1103/PhysRevE.101.052603](https://doi.org/10.1103/PhysRevE.101.052603)

### I. INTRODUCTION

Ionic interactions in aqueous solution play a pivotal role in numerous processes of biological and technological relevance. The adsorption of proteins or DNA onto lipid membranes [1–4], the rate of aggregation of colloidal particles [5,6], the development of efficient methods to desalinate water [7,8], and the optimization of energy-storage devices [9–12] are a few among many examples that involve interacting macroions (or charged interfaces) in aqueous solutions. All these interactions depend crucially on the formation of a diffuse layer of co- and counterions, commonly referred to as the electric double layer [13]. It is thus no surprise that the electric double layer has been the subject of extensive theoretical modeling, leading initially to the development of the classical Poisson-Boltzmann theory [14,15] and subsequently to many practical applications [16–21] and extensions that address the two main shortcomings of the classical model: the treatment of all ions as pointlike charges and the neglect of ion-ion correlations [22–24]. These extensions account (often in an approximate manner) for the shape and steric size of the ions [25–27], dipolar interactions [28,29], van der Waals interactions [30], ion-mediated modifications of the dielectric constant [31], and structure of the solvent [32]. Many of these modeling efforts are motivated by the difficulty to rationalize experimentally observed ion-specific effects [33,34].

Ions in aqueous solution experience additional nonelectrostatic interactions, hydration interactions, that are ion-specific,

mediated by the solvent, and rooted in the ion-induced ordering of water molecules [35–41]. Solvent-mediated surface-surface, ion-surface, and ion-ion interactions are soft and characterized by a decay length roughly equal to the molecular size of water [42]. Furthermore, hydration interactions often exhibit oscillatory behavior [43] that is affected by the electrolyte type and concentration, as suggested by the atomic force microscopy force-distance measurements performed by Moghaddam and Thormann [44] for coated gold surfaces in 200 mM of NaF and by van Lin *et al.* [45] for mica surfaces in various alkali-metal chloride solutions. The oscillatory nature of the potential is also supported by detailed molecular dynamics and Monte Carlo simulations carried out by Dzubiella and co-workers, who suggest that ion-ion [46] and ion-surface potentials [47] are short ranged and characterized by damped electrolyte-dependent oscillations. While the exclusive presence of oscillating potentials has been studied in the past [48], no mean-field framework exists yet for their presence in conjunction with the Coulomb potential.

One specific method of incorporating solvent-mediated interactions into mean-field electrostatics of the electric double layer is by adding a Yukawa potential to the Coulomb potential between two ions [49–51]. The Yukawa potential is soft and short ranged, and it connects mean-field electrostatics to a phenomenological model for solvent-mediated interactions proposed by Marčelja and Radić [52]. A mean-field formalism was previously proposed [53] and then generalized [54] that accounts consistently for ion-ion, ion-surface, and

surface-surface interactions. The nonoscillating Yukawa potential is added to the Coulomb potential in an ion-specific manner, thus allowing anion-anion, anion-cation, and cation-cation pairs to interact differently depending on their ability to affect the solvent structure.

Oscillating Yukawa potentials regularly appear in modeling electrostatic screening effects in plasmas, where they arise from correlation effects [55–57]. They have not yet been used to describe nonelectrostatic solvent-mediated interactions between ions in electrolytes, where they appear in addition to (and not as an effective ion-ion potential instead of) the long-ranged Coulomb potential. Here only monotonic Yukawa potentials have been studied [58] and compared with results from corresponding Monte Carlo simulations [59,60]. Yet, as argued above, available experimental and computational evidence suggests that solvent-mediated potentials exhibit damped oscillations. Hence, in the present work, we extend the use of monotonic Yukawa potentials to non-monotonic ones by allowing the inverse decay length  $\kappa$  in the Yukawa potential  $e^{-\kappa r}/r$  (where  $r$  denotes the ion-to-ion distance) to adopt complex values. Our goal is to present a comprehensive model with individualized oscillating Yukawa contributions to the total anion-anion, anion-cation, and cation-cation interaction potentials. Our model also includes ion-specific interactions of ions with surfaces of macroions that are present in the aqueous solution. We exemplify possible applications of our model by calculating the differential capacitance of a single planar electrode and the pressure between two planar, like-charged macroion surfaces.

## II. THEORY

Consider a symmetric 1:1 electrolyte with local volume fraction  $\phi_a = \phi_a(\mathbf{r})$  of anions and  $\phi_c = \phi_c(\mathbf{r})$  of cations. The electrolyte with all its microions takes up a sufficiently large space of volume  $V_e$  so that it forms a bulk solution in all spatial directions, and it contains one or more macroions of total volume  $V_m$  and surface area  $A$ . The combined volume  $V = V_e + V_m$  denotes all space. We assume each individual anion and cation occupies the same volume  $\nu$  and we denote the bulk volume fractions of the anions and cations by  $\phi_0$ , that is,  $\phi_0 = \phi_a(|\mathbf{r}| \rightarrow \infty) = \phi_c(|\mathbf{r}| \rightarrow \infty)$ . Figure 1 shows a schematic illustration of an electrolyte with two macroions.

Any two ions experience a mutual interaction as a function of their center-to-center distance  $r$  that is composed of an electrostatic and a hydration-mediated component, where the latter is modeled as an oscillating Yukawa potential. Specifically, we express the anion-anion ( $u_{aa}$ ), anion-cation ( $u_{ac}$ ), and cation-cation ( $u_{cc}$ ) pair potentials as

$$\begin{aligned} \frac{u_{aa}}{k_B T} &= \frac{l_B}{r} + a \frac{e^{-\kappa_r r}}{r} \cos(\kappa_c r + \alpha), \\ \frac{u_{ac}}{k_B T} &= -\frac{l_B}{r} + b \frac{e^{-\kappa_r r}}{r} \cos(\kappa_c r + \beta), \\ \frac{u_{cc}}{k_B T} &= \frac{l_B}{r} + c \frac{e^{-\kappa_r r}}{r} \cos(\kappa_c r + \gamma), \end{aligned} \quad (1)$$

where  $l_B (= e^2/4\pi\epsilon_0\epsilon_w k_B T)$  denotes the Bjerrum length, with the elementary charge  $e$ , vacuum permittivity  $\epsilon_0$ , dielectric constant of water  $\epsilon_w$ , Boltzmann constant  $k_B$ , and absolute

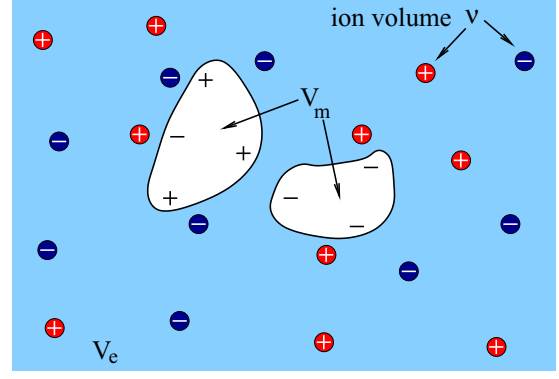


FIG. 1. Schematic illustration of two macroions contained in a symmetric 1:1 electrolyte. The volume  $V_e$  of the electrolyte is sufficiently large so that a bulk exists in all spatial directions. The total volume of the macroions is denoted by  $V_m$ . All microions (anions and cations) have the same volume  $\nu$ .

temperature  $T$ . The parameter  $\kappa_r^{-1}$  characterizes the decay length of the Yukawa potential and  $2\pi\kappa_c^{-1}$  the period length of the oscillation. The Yukawa interaction strengths  $a$ ,  $b$ , and  $c$  as well as the phases  $\alpha$ ,  $\beta$ , and  $\gamma$  embody the ion specificity of the hydration-mediated interactions.

Our goal is to develop and analyze a mean-field model based on the ion-ion pair interactions in Eqs. (1). To this end, we define three dimensionless potentials  $\Psi_e(\mathbf{r})$ ,  $\Psi_a(\mathbf{r})$ , and  $\Psi_c(\mathbf{r})$  at position  $\mathbf{r}$  anywhere in space. The first one,

$$\Psi_e(\mathbf{r}) = \frac{l_B}{\nu} \int_{V_e} d^3\mathbf{r}' \frac{\phi_c(\mathbf{r}') - \phi_a(\mathbf{r}')}{|\mathbf{r} - \mathbf{r}'|}, \quad (2)$$

is the (real-valued) electrostatic potential and the other two,

$$\begin{pmatrix} \Psi_a(\mathbf{r}) \\ \Psi_c(\mathbf{r}) \end{pmatrix} = \frac{1}{\nu} \int_{V_e} d^3\mathbf{r}' \frac{e^{-\kappa|\mathbf{r}-\mathbf{r}'|}}{|\mathbf{r} - \mathbf{r}'|} \mathcal{A}_h \begin{pmatrix} \phi_a(\mathbf{r}') - \phi_0 \\ \phi_c(\mathbf{r}') - \phi_0 \end{pmatrix}, \quad (3)$$

describe the oscillating Yukawa interactions. In Eq. (3) we have cast the interaction strengths  $a$ ,  $b$ , and  $c$  and phase factors  $\alpha$ ,  $\beta$ , and  $\gamma$  into the form of a complex-valued matrix

$$\mathcal{A}_h = \begin{pmatrix} ae^{i\alpha} & be^{i\beta} \\ be^{i\beta} & ce^{i\gamma} \end{pmatrix} = \begin{pmatrix} \tilde{a} & \tilde{b} \\ \tilde{b} & \tilde{c} \end{pmatrix}, \quad (4)$$

thus introducing the definitions  $\tilde{a} = ae^{i\alpha}$ ,  $\tilde{b} = be^{i\beta}$ , and  $\tilde{c} = ce^{i\gamma}$ . We have also defined the complex-valued inverse decay length

$$\kappa = \kappa_r + i\kappa_c, \quad (5)$$

implying that the two hydration potentials

$$\Psi_a = \eta_a + i\tau_a, \quad \Psi_c = \eta_c + i\tau_c \quad (6)$$

are complex valued. In Eqs. (2) and (3) we have ignored any sources of the potentials  $\Psi_e(\mathbf{r})$ ,  $\Psi_a(\mathbf{r})$ , and  $\Psi_c(\mathbf{r})$  that may be present at the macroion surfaces; these will be accounted for below in Eqs. (17).

Equations (2) and (3) can be reexpressed in local form as partial differential equations: the Poisson equation for the electrostatic potential

$$l^2 \nabla^2 \Psi_e = \phi_a - \phi_c, \quad (7)$$

with the differential operator  $\nabla$  (so that  $\nabla^2$  is the Laplacian) and  $l^2 = \nu/4\pi l_B$ , and two screened Poisson equations (with complex-valued screening constant) for the two hydration potentials

$$\begin{pmatrix} (\nabla^2 - \kappa^2)\Psi_a \\ (\nabla^2 - \kappa^2)\Psi_c \end{pmatrix} = -\frac{4\pi}{\nu} \mathcal{A}_h \begin{pmatrix} \phi_a - \phi_0 \\ \phi_c - \phi_0 \end{pmatrix}. \quad (8)$$

The total interaction energy  $U = U_{el} + U_h$  is the sum of an electrostatic contribution

$$\frac{U_{el}}{k_B T} = \frac{1}{2\nu} \int_{V_e} d^3\mathbf{r} \Psi_e(\phi_c - \phi_a) \quad (9)$$

and a hydration contribution

$$\frac{U_h}{k_B T} = \frac{1}{2\nu} \int_{V_e} d^3\mathbf{r} \begin{pmatrix} \eta_a \\ \eta_c \end{pmatrix}^\top \begin{pmatrix} \phi_a - \phi_0 \\ \phi_c - \phi_0 \end{pmatrix}, \quad (10)$$

where the superscript  $\top$  denotes the transpose of a matrix (here, column vector). Note that because  $\eta_a = (\Psi_a + \Psi_a^*)/2$  and  $\eta_c = (\Psi_c + \Psi_c^*)/2$  are real valued (the star superscript denotes the complex conjugate), the energy  $U_h$  is real valued. Using Eqs. (7) and (8), we can express the interaction energies  $U_{el}$  and  $U_h$  exclusively in terms of the three potentials  $\Psi_e$ ,  $\Psi_a = \eta_a + i\tau_a$ , and  $\Psi_c = \eta_c + i\tau_c$ ,

$$\frac{U_{el}}{k_B T} = \frac{l^2}{2\nu} \int_{V_e} d^3\mathbf{r} (\nabla \Psi_e)^2, \quad (11a)$$

$$\begin{aligned} \frac{U_h}{k_B T} = & \frac{1}{8\pi} \int_{V_e} d^3\mathbf{r} \frac{1}{2} \left[ \begin{pmatrix} \nabla \Psi_a \\ \nabla \Psi_c \end{pmatrix}^\top \mathcal{A}_h^{-1} \begin{pmatrix} \nabla \Psi_a \\ \nabla \Psi_c \end{pmatrix} \right. \\ & \left. + \kappa^2 \begin{pmatrix} \Psi_a \\ \Psi_c \end{pmatrix}^\top \mathcal{A}_h^{-1} \begin{pmatrix} \Psi_a \\ \Psi_c \end{pmatrix} + \text{c.c.} \right], \quad (11b) \end{aligned}$$

where the integrations run over all space and  $\mathcal{A}_h^{-1}$  denotes the inverse of  $\mathcal{A}_h$ . At this point, we assume the inverse exists. The degenerate case of a vanishing determinant,  $\det \mathcal{A}_h = 0$ , will be treated in Sec. II. In Eqs. (11) and below we use the notation +c.c. to denote the complex conjugate of all terms inside the square brackets, that is,  $[x + iy + \text{c.c.}] = 2x$  for real numbers  $x$  and  $y$ . We note that the interaction energy  $U_h$  in Eq. (11b) can be expressed equivalently as

$$\begin{aligned} \frac{U_h}{k_B T} = & \frac{1}{8\pi} \int_{V_e} d^3\mathbf{r} \frac{1}{2} \left[ \begin{pmatrix} \nabla \Psi_a^* \\ \nabla \Psi_c^* \end{pmatrix}^\top (\mathcal{A}_h^{-1*} + \mathcal{A}_h^{-1}) \begin{pmatrix} \nabla \Psi_a \\ \nabla \Psi_c \end{pmatrix} \right. \\ & \left. + \begin{pmatrix} \Psi_a^* \\ \Psi_c^* \end{pmatrix}^\top (\kappa^2 \mathcal{A}_h^{-1} + \kappa^{2*} \mathcal{A}_h^{-1*}) \begin{pmatrix} \Psi_a \\ \Psi_c \end{pmatrix} \right], \quad (12) \end{aligned}$$

but for the derivation of the equilibrium ion distribution (as outlined below) we have found it more convenient to use  $U_h$  in Eq. (11b). To develop our mean-field model we need to specify an entropy contribution associated with the demixing of the ions in the electrolyte. While the most simple approach employs an ideal gas mixing entropy, here we will use a lattice

gas description

$$\begin{aligned} S = & -\frac{k_B}{\nu} \int_{V_e} d^3\mathbf{r} \left[ \phi_a \ln \frac{\phi_a}{\phi_0} + \phi_c \ln \frac{\phi_c}{\phi_0} \right. \\ & \left. + (1 - \phi_a - \phi_c) \ln \frac{1 - \phi_a - \phi_c}{1 - 2\phi_0} \right], \quad (13) \end{aligned}$$

which offers the advantage of limiting the total ion volume fraction  $\phi_a + \phi_c \leq 1$  without giving up mathematical convenience [25].

The free energy of the electrolyte  $F = U - TS$ , with  $U$  and  $S$  according to Eqs. (11) and (13), represents a functional  $F[\phi_a, \phi_c, \Psi_e(\phi_a, \phi_c), \Psi_a(\phi_a, \phi_c), \Psi_c(\phi_a, \phi_c)]$  in terms of the yet unknown volume fractions  $\phi_a$  and  $\phi_c$ . The implicit dependences of the potentials on  $\phi_a$  and  $\phi_c$  in that functional are specified by the Poisson and screened Poisson equations [see Eqs. (7) and (8)]. Hence, we can carry out a variation  $\delta F$  of the free energy  $F$  with respect to  $\phi_a$  and  $\phi_c$ . Vanishing of the variation  $\delta F = 0$  determines the distributions that  $\phi_a$  and  $\phi_c$  adopt in thermal equilibrium,

$$\phi_a = \frac{\phi_0}{q} e^{\Psi_e - \eta_a}, \quad \phi_c = \frac{\phi_0}{q} e^{-\Psi_e - \eta_c}, \quad (14)$$

where the factor

$$q = 1 + \phi_0 (e^{\Psi_e - \eta_a} + e^{-\Psi_e - \eta_c} - 2) \quad (15)$$

ensures the saturation condition  $\phi_a + \phi_c \leq 1$  of this distribution, which (as pointed out by Kornyshev [26]) is reminiscent of a Fermi distribution. We note that  $\phi_a$  and  $\phi_c$  in Eqs. (14) are real valued because they depend only on  $\Psi_e$ ,  $\eta_a = (\Psi_a + \Psi_a^*)/2$ , and  $\eta_c = (\Psi_c + \Psi_c^*)/2$ .

Inserting the distributions for  $\phi_a$  and  $\phi_c$  according to Eqs. (14) into the Poisson and screened Poisson equations (7) and (8) results in a set of three coupled differential equations

$$l^2 \nabla^2 \Psi_e = \frac{\phi_0}{q} (e^{\Psi_e - \eta_a} - e^{-\Psi_e - \eta_c}), \quad (16a)$$

$$\begin{pmatrix} (\nabla^2 - \kappa^2)\Psi_a \\ (\nabla^2 - \kappa^2)\Psi_c \end{pmatrix} = -\frac{4\pi}{\nu} \frac{\phi_0}{q} \mathcal{A}_h \begin{pmatrix} e^{\Psi_e - \eta_a} - q \\ e^{-\Psi_e - \eta_c} - q \end{pmatrix} \quad (16b)$$

for the potentials  $\Psi_e$ ,  $\Psi_a = \eta_a + i\tau_a$ , and  $\Psi_c = \eta_c + i\tau_c$ . We refer to them as the Poisson-Fermi and screened Poisson-Fermi equations. Note that we follow Kornyshev [26,61] in using the term ‘‘Poisson-Fermi,’’ which reflects the Fermi-like distribution that arises from using an underlying lattice model to approximate the excluded volume of the ions. The Poisson-Fermi equation (16a) is real valued, whereas the two screened Poisson-Fermi equations involve the two complex-valued potentials  $\Psi_a$  and  $\Psi_c$  as well as the complex-valued  $\kappa$  and  $\mathcal{A}_h$ .

Equations (16) must be solved within the space  $V_e$  occupied by the electrolyte. Inside the macroions, the same equations, yet with vanishing right-hand sides, must be solved. That is, inside  $V_m$ , the potentials fulfill the three decoupled linear equations  $\nabla^2 \Psi_e = 0$ ,  $\nabla^2 \Psi_a = \kappa^2 \Psi_a$ , and  $\nabla^2 \Psi_c = \kappa^2 \Psi_c$ . Very far away from the electrolyte, for  $|\mathbf{r}| \rightarrow \infty$ , all three potentials vanish. When crossing the macroion surfaces, the three potentials remain continuous. If the macroion surfaces contain sources for the electrostatic or for the Yukawa interactions, the

derivatives of the potentials change discontinuously. Mathematically, this is expressed through the boundary conditions

$$-\left(\frac{\partial\Psi_e}{\partial n}\right)_{A_{\text{in}}} = 4\pi l_B \frac{\sigma_e}{e}, \quad (17a)$$

$$\left(\frac{\partial\Psi_a}{\partial n}\right)_{A_{\text{out}}} - \left(\frac{\partial\Psi_a}{\partial n}\right)_{A_{\text{in}}} = 4\pi\mathcal{A}_h \begin{pmatrix} \sigma_a e^{i\theta_a} \\ \sigma_c e^{i\theta_c} \end{pmatrix}, \quad (17b)$$

where  $\sigma_e$  is the electric surface charge density,  $\sigma_a$  and  $\sigma_c$  are the surface densities of sources for the hydration-mediated interaction,  $\theta_a$  and  $\theta_c$  are phase factors,  $(\frac{\partial}{\partial n})_{A_{\text{in}}}$  is the normal derivative at the macroion surface into the direction of the electrolyte, and  $(\frac{\partial}{\partial n})_{A_{\text{out}}}$  is the normal derivative at the macroion surface away from the electrolyte into the macroion. The boundary condition for the electrostatic potential (17a) also assumes that the dielectric constant inside the macroions is much smaller than that of water. We emphasize again that the boundary conditions involving the potentials  $\Psi_a = \eta_a + i\tau_a$  and  $\Psi_c = \eta_c + i\tau_c$  are complex valued. The four quantities  $\sigma_a$ ,  $\theta_a$ ,  $\sigma_c$ , and  $\theta_c$  can be used to define any magnitude and phase relationship for the interaction of the anions and cations in solution with the macroion surface.

Upon inserting the distributions for  $\phi_a$  and  $\phi_c$  according to Eqs. (14) into the free energy  $F = U - TS$  [with  $U$  and  $S$  specified in Eqs. (11) and (13)] we obtain

$$\begin{aligned} \frac{F}{k_B T} = & \int_A d^2\mathbf{r} \left[ \Psi_e \frac{\sigma_e}{e} + \begin{pmatrix} \sigma_a \\ \sigma_c \end{pmatrix}^\top \begin{pmatrix} \eta_a \cos \theta_a - \tau_a \sin \theta_a \\ \eta_c \cos \theta_c - \tau_c \sin \theta_c \end{pmatrix} \right] \\ & - \frac{1}{v} \int_V d^3\mathbf{r} \left\{ \frac{l^2}{2} (\nabla\Psi_e)^2 + \frac{v}{8\pi} \frac{1}{2} \left[ \begin{pmatrix} \nabla\Psi_a \\ \nabla\Psi_c \end{pmatrix}^\top \mathcal{A}_h^{-1} \begin{pmatrix} \nabla\Psi_a \\ \nabla\Psi_c \end{pmatrix} \right. \right. \\ & \left. \left. + \kappa^2 \begin{pmatrix} \Psi_a \\ \Psi_c \end{pmatrix}^\top \mathcal{A}_h^{-1} \begin{pmatrix} \Psi_a \\ \Psi_c \end{pmatrix} + \text{c.c.} \right] \right\} \\ & - \frac{1}{v} \int_{V_e} d^3\mathbf{r} [\ln q + \phi_0(\eta_a + \eta_c)], \quad (18) \end{aligned}$$

where the first integration runs over the macroion surfaces  $A$ , the second integration runs over the electrolyte and the macroions, and the third integration runs over the electrolyte only. The free energy  $F(\Psi_e, \Psi_a, \Psi_c)$  in Eq. (18) represents a functional that depends exclusively on the three potentials  $\Psi_e$ ,  $\Psi_a$ , and  $\Psi_c$ . Vanishing of its variation  $\delta F(\Psi_e, \Psi_a, \Psi_c) = 0$  yields exactly the mean-field equations [the Poisson-Fermi and screened Poisson-Fermi equations specified in Eqs. (16)] and the corresponding boundary conditions in Eqs. (17). Hence, Eq. (18) provides a complete mean-field lattice gas description of the electric double layer in the presence of both Coulomb and oscillating Yukawa interactions. This description is valid for any number of involved macroions, irrespective of their geometries.

#### Degenerate case $\tilde{b} = \pm\sqrt{\tilde{a}\tilde{c}}$

The square matrix  $\mathcal{A}_h$  in Eq. (4) characterizes the strengths of the hydration interactions. The choices  $b = \pm\sqrt{ac}$  and  $\beta = (\alpha + \gamma)/2$  imply  $\tilde{b} = be^{i\beta} = \pm\sqrt{\tilde{a}\tilde{c}}$ ; this renders the matrix  $\mathcal{A}_h$  degenerate (also called noninvertible or singular), with

vanishing determinant,  $\det \mathcal{A}_h = 0$ . Note that positive and negative  $b$  correspond to hydration-mediated repulsion and attraction, respectively, between an anion and a cation.

If the matrix  $\mathcal{A}_h$  is degenerate, the two hydration potentials are no longer independent. It is then appropriate to define a single complex-valued hydration potential  $\Psi_h = \eta + i\tau$  through

$$\begin{aligned} \Psi_h(\mathbf{r}) = & \frac{(ac)^{1/4}}{v} \int_{V_e} d^3\mathbf{r}' \frac{e^{-\kappa|\mathbf{r}-\mathbf{r}'|}}{|\mathbf{r}-\mathbf{r}'|} \\ & \times \{\sqrt{\tilde{a}}[\phi_a(\mathbf{r}') - \phi_0] \pm \sqrt{\tilde{c}}[\phi_c(\mathbf{r}') - \phi_0]\}. \quad (19) \end{aligned}$$

The complex nature of  $\Psi_h$  emerges because  $\kappa = \kappa_r + i\kappa_c$ ,  $\tilde{a} = ae^{i\alpha}$ , and  $\tilde{c} = ce^{i\gamma}$  are complex valued. In Eq. (19) and below, the upper and lower signs in  $\pm$  or  $\mp$  refer to  $b > 0$  and  $b < 0$ , respectively. When  $\Psi_h$  is inserted into the hydration interaction energy

$$\begin{aligned} \frac{U_h}{k_B T} = & \frac{1}{2v(ac)^{1/4}} \times \frac{1}{2} \int_{V_e} d^3\mathbf{r} \{ \Psi_h(\mathbf{r}) \times \\ & \times [\sqrt{\tilde{a}}(\phi_a - \phi_0) \pm \sqrt{\tilde{c}}(\phi_c - \phi_0)] + \text{c.c.} \}, \quad (20) \end{aligned}$$

the degenerate case  $\tilde{b} = \pm\sqrt{\tilde{a}\tilde{c}}$  is properly accounted for. As for the nondegenerate case, we can cast the potential  $\Psi_h$  into a local form

$$\begin{aligned} l_h^2(\nabla^2 - \kappa^2)\Psi_h = & - \left[ \left(\frac{a}{c}\right)^{1/4} e^{i\alpha/2}(\phi_a - \phi_0) \right. \\ & \left. \pm \left(\frac{c}{a}\right)^{1/4} e^{i\gamma/2}(\phi_c - \phi_0) \right], \quad (21) \end{aligned}$$

where we have defined the length  $l_h$  through

$$l_h^2 = \frac{v}{4\pi\sqrt{ac}}. \quad (22)$$

Equation (21) constitutes the screened Poisson equation for the degenerate case. Inserting the screened Poisson equation into  $U_h$  allows us to express the hydration energy exclusively in terms of the hydration potential,

$$\frac{U_h}{k_B T} = \frac{l_h^2}{2v} \left(\frac{1}{2}\right) \int_V d^3\mathbf{r} \{ [(\nabla\Psi_h)^2 + \kappa^2\Psi_h^2] + \text{c.c.} \}. \quad (23)$$

Minimization of the free energy  $F = U_{el} + U_h - TS$  [with  $U_{el}$  from Eq. (11a),  $U_h$  from Eq. (23), and  $S$  according to Eq. (13)], subject to the Poisson equation (7) and the screened Poisson equation (21), reproduces exactly the equilibrium ion distributions in Eqs. (14) [with  $q$  specified in Eq. (15)], yet with

$$\begin{aligned} \eta_a = & \left(\frac{a}{c}\right)^{1/4} \left( \eta \cos \frac{\alpha}{2} - \tau \sin \frac{\alpha}{2} \right), \\ \eta_c = & \pm \left(\frac{c}{a}\right)^{1/4} \left( \eta \cos \frac{\gamma}{2} - \tau \sin \frac{\gamma}{2} \right). \quad (24) \end{aligned}$$

In the following we continue to use  $\eta_a$  and  $\eta_c$  and identify them with the expressions in Eqs. (24). Inserting the equilibrium ion distributions for  $\phi_a$  and  $\phi_c$  from Eqs. (14) into the Poisson and screened Poisson equations (7) and (21) gives rise to the Poisson-Fermi and screened Poisson-Fermi equations

for the degenerate case

$$\begin{aligned}
 l^2 \nabla^2 \Psi_e &= \frac{\phi_0}{q} (e^{\Psi_e - \eta_a} - e^{-\Psi_e - \eta_c}), \\
 l_h^2 (\nabla^2 - \kappa^2) \Psi_h &= -\phi_0 \left[ \left( \frac{a}{c} \right)^{1/4} e^{i\alpha/2} \left( \frac{e^{\Psi_e - \eta_a}}{q} - 1 \right) \right. \\
 &\quad \left. \pm \left( \frac{c}{a} \right)^{1/4} e^{i\gamma/2} \left( \frac{e^{-\Psi_e - \eta_c}}{q} - 1 \right) \right]. \quad (25)
 \end{aligned}$$

They fulfill the boundary conditions

$$\begin{aligned}
 -l^2 \left( \frac{\partial \Psi_e}{\partial n} \right)_{A_{\text{in}}} &= v \frac{\sigma_e}{e}, \\
 l_h^2 \left[ \left( \frac{\partial \Psi_h}{\partial n} \right)_{A_{\text{out}}} - \left( \frac{\partial \Psi_h}{\partial n} \right)_{A_{\text{in}}} \right] &= v \sigma_h e^{i\theta_h}, \quad (26)
 \end{aligned}$$

where the density of sources  $\sigma_h$  and the corresponding phase factor  $\theta_h$  for the hydration-mediated interaction in the degenerate case are related to the values  $\sigma_a e^{i\theta_a}$  and  $\sigma_c e^{i\theta_c}$  for the nondegenerate case via

$$e^{i\theta_h} \sigma_h = \left( \frac{a}{c} \right)^{1/4} e^{i(\alpha/2 + \theta_a)} \sigma_a \pm \left( \frac{c}{a} \right)^{1/4} e^{i(\gamma/2 + \theta_c)} \sigma_c. \quad (27)$$

Finally, the free-energy functional  $F(\Psi_e, \Psi_h)$  that yields the Poisson-Fermi and screened Poisson-Fermi equations (25) as well as the corresponding boundary conditions (26) as its stationary state reads, for the degenerate case,

$$\begin{aligned}
 \frac{F}{k_B T} &= \int_A d^2 \mathbf{r} \left[ \Psi_e \frac{\sigma_e}{e} + \sigma_h (\eta \cos \theta_h - \tau \sin \theta_h) \right] \\
 &\quad - \frac{1}{v} \int_V d^3 \mathbf{r} \frac{l^2}{2} (\nabla \Psi_e)^2 \\
 &\quad - \frac{1}{v} \left( \frac{1}{2} \right) \int_V d^3 \mathbf{r} \left\{ \frac{l_h^2}{2} [(\nabla \Psi_h)^2 + \kappa^2 \Psi_h^2] + \text{c.c.} \right\} \\
 &\quad - \frac{1}{v} \int_V d^3 \mathbf{r} [\ln q + \phi_0 (\eta_a + \eta_c)]. \quad (28)
 \end{aligned}$$

This completes our goal of developing a mean-field model for ion-ion pair potentials that are composed of an electrostatic and an oscillating Yukawa component. The model we presented is valid for any choices of the hydration interaction strengths  $a$ ,  $b$ , and  $c$  and phase factors  $\alpha$ ,  $\beta$ , and  $\gamma$ . The local hydration properties of a macroion surface are fully specified by the two source densities  $\sigma_a$  and  $\sigma_c$  and corresponding phases  $\theta_a$  and  $\theta_c$ .

### III. RESULTS AND DISCUSSION

To illustrate our general approach, we study two macroions that have flat parallel surfaces facing each other as shown in Fig. 2. Each of the two planar macroion surfaces is of sufficiently large lateral area  $A$  so that finite-size effects can be neglected. They are separated by a distance  $d$  and each carries the same set of sources  $\sigma_e$  and  $\sigma_h$  (or  $\sigma_e$ ,  $\sigma_a$ , and  $\sigma_c$  for the nondegenerate case). We assume that the phase of the hydration source on the electrode surface vanishes  $\theta_h = 0$  (or  $\theta_a = \theta_c = 0$  for the nondegenerate case). Hence not only are the two macroions like charged, they also have the same

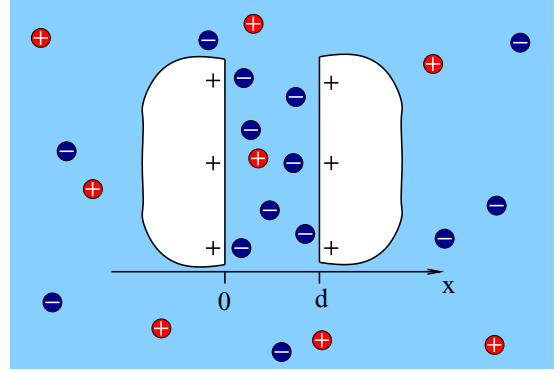


FIG. 2. Same system as in Fig. 1, yet with the two macroions having large planar and parallel faces, located at positions  $x = 0$  and  $x = d$  along the  $x$  axis, which points normal to the two flat surfaces. The system we consider exhibits symmetry across the plane  $x = d/2$ .

hydration properties. On the mean-field level, the electrolyte properties vary only along the direction normal to the two flat surfaces, which we identify with the  $x$  axis of a Cartesian coordinate system. Differential operators can then be replaced by corresponding derivatives along the  $x$  direction, that is,  $\nabla \Psi_e \rightarrow \Psi_e'(x)$ , etc. The two surfaces are located at positions  $x = 0$  and  $x = d$  (see Fig. 2). Because both macroions are identical, with the same  $\sigma_e$  and  $\sigma_h$  (the same  $\sigma_a$  and  $\sigma_c$  for the nondegenerate case), all potentials are symmetric across the surface  $x = d/2$ .

We are interested in two quantities. The first is the differential capacitance  $C^{\text{diff}} = d\sigma_e/d\Phi_0$  of an isolated planar surface, where  $\Phi_0 = \Psi_e(0)k_B T/e$  is the electrostatic surface potential (measured in volts) of the surface located at  $x = 0$ . To this end, we consider the limit  $d \rightarrow \infty$  and compute the dimensionless electrostatic surface potential  $\Psi_e(0)$  as a function of  $\sigma_e$ , with all other parameters being fixed. Note that in the complete absence of hydration interactions, we recover the well-known [26] lattice gas result

$$\bar{C}^{\text{diff}} = \frac{\sqrt{(1 - e^{4\phi_0 w^2})(1 - e^{4\phi_0 w^2} - 4\phi_0)}}{4\phi_0 w e^{4\phi_0 w^2}} \quad (29)$$

for the scaled (dimensionless) differential capacitance  $\bar{C}^{\text{diff}} = l_D C^{\text{diff}} / \epsilon_w \epsilon_0$ , expressed in terms of the scaled surface charge density  $w = 2\pi l_B l_D \sigma_e / e$ , where  $l_D = l / \sqrt{2\phi_0}$  denotes the Debye screening length. At a bulk volume fraction  $\phi_0 = 1/6$  of the ions, Eq. (29) predicts the transition from camel-shaped (for  $\phi_0 < 1/6$ ) to bell-shaped (for  $\phi_0 > 1/6$ ) profiles. One of our goals is to characterize how the presence of an oscillating Yukawa potential modifies the result in Eq. (29).

The second quantity is the pressure  $P$  that acts between the two macroion surfaces as a function of their separation  $d$ . To calculate the pressure, we perform a Legendre transformation  $G = F + PV$ , where  $V = Ad$  is the volume enclosed between the two planar surfaces and  $F$  the free energy according to Eq. (18). Because the functional  $G$  does not explicitly depend on  $x$ , we can use the Beltrami identity to identify the pressure as a constant of integration

$$\frac{Pv}{k_B T} = \ln q + \phi_0(\eta_a + \eta_c) - \frac{l^2}{2}(\Psi'_e)^2 - \frac{v}{8\pi} \left(\frac{1}{2}\right) \times \left[ \begin{pmatrix} \Psi'_a \\ \Psi'_c \end{pmatrix}^\top \mathcal{A}_h^{-1} \begin{pmatrix} \Psi'_a \\ \Psi'_c \end{pmatrix} - \kappa^2 \begin{pmatrix} \Psi_a \\ \Psi_c \end{pmatrix}^\top \mathcal{A}_h^{-1} \begin{pmatrix} \Psi_a \\ \Psi_c \end{pmatrix} + \text{c.c.} \right], \quad (30)$$

where  $q$  is specified in Eq. (15). For the degenerate case, the same calculation yields

$$\frac{Pv}{k_B T} = \ln q + \phi_0(\eta_a + \eta_c) - \frac{l^2}{2}(\Psi'_e)^2 - \frac{l_h^2}{2} \left(\frac{1}{2}\right) [(\Psi'_h)^2 - \kappa^2 \Psi_h^2 + \text{c.c.}], \quad (31)$$

where we recall that  $\eta_a$  and  $\eta_c$  are specified in Eqs. (24). The pressure  $P$  can be calculated at any position  $x$  between the two macroion surfaces.

In the following, we study two specific scenarios that both belong to the degenerate case:  $a = b = c$  and  $a = -b = c$ . In the former case, for  $a = b = c$ , all anion-anion, anion-cation, and cation-cation pairs experience the same hydration-mediated repulsion. In the latter case, for  $a = -b = c$ , the hydration-mediated anion-cation interaction is attractive. In all of the following we assume vanishing phase factors  $\alpha = \beta = \gamma = 0$ .

Throughout this work, we fix the Bjerrum length  $l_B = 0.7$  nm and the bulk ion concentration  $n_0 = \phi_0/v = 0.057$  nm<sup>-3</sup>. This produces a Debye screening length of  $l_D = (8\pi l_B \phi_0/v)^{-1/2} = 1$  nm and corresponds to a 100 mM salt solution. In addition, we choose a density  $\sigma_h = 5$  nm<sup>-2</sup> for the sources of the hydration interaction on the electrode surface; this reflects roughly the density of water molecules [58]. Simulation results presented by Dzubiella and co-workers [46,47] suggest to use the generic values  $a = 1$  nm,  $\kappa_r = 3.33$  nm<sup>-1</sup>, and  $\kappa_c = 12.5$  nm<sup>-1</sup> as parameters for the oscillating Yukawa potential. These simulations also provide a rationale for our choice  $\alpha = \beta = \gamma = 0$  introduced above. Figure 3 shows the oscillating Yukawa potential  $ae^{-\kappa_r r} \cos(\kappa_c r)/r$  (blue solid line) together with the composite potential  $ae^{-\kappa_r r} \cos(\kappa_c r)/r + l_B/r$  (light blue dashed line). To visualize the role of the oscillatory component, we have added to Fig. 3 plots that correspond to  $\kappa_c = 0$ ; we show the Yukawa potential  $ae^{-\kappa_r r}/r$  (red solid line) and the ensuing composite potential  $ae^{-\kappa_r r}/r + l_B/r$  (light red dashed line). The main diagram in Fig. 3 corresponds to anion-anion or cation-cation pairs. The inset displays the same set of potentials, yet for an anion-cation pair. The difference between corresponding dashed and solid lines equals  $l_B/r$  in the main diagram and  $-l_B/r$  in the inset.

Note the two local minima close to  $r = 0.2$  nm of the composite oscillating potentials (light blue dashed lines in the main diagram and inset): Anion-anion or cation-cation pairs exhibit a metastable equilibrium separation and anion-cation pairs a strongly bound state. In the absence of the oscillatory component, for  $\kappa_c = 0$ , anion-anion or cation-cation pairs always repel each other whereas anion-cation pairs exhibit a weakly bound state at  $r = 0.33$  nm (light red dashed lines in the main diagram and inset).

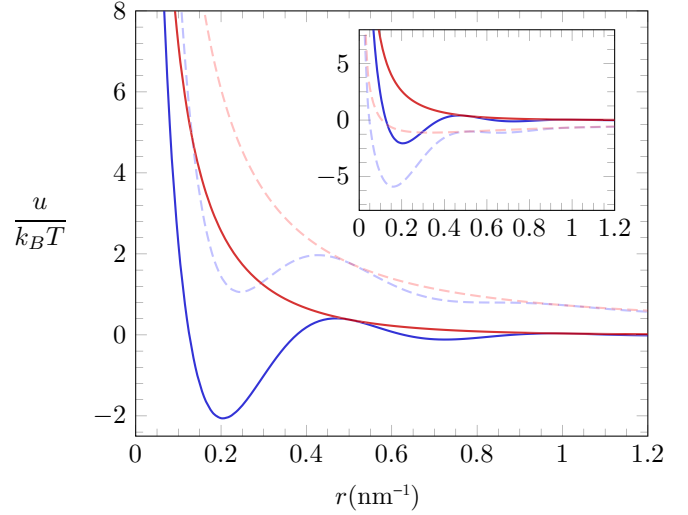


FIG. 3. Yukawa potential  $ae^{-\kappa_r r} \cos(\kappa_c r)/r$  (blue solid line) and composite potential  $ae^{-\kappa_r r} \cos(\kappa_c r)/r + l_B/r$  (light blue dashed line) for anion-anion or cation-cation pairs, with  $a = 1$  nm,  $\kappa_r = 3.33$  nm<sup>-1</sup>,  $\kappa_c = 12.5$  nm<sup>-1</sup>, and  $l_B = 0.7$  nm. The two red lines refer to the Yukawa potential without the oscillatory component  $ae^{-\kappa_r r}/r$  (red solid line) and the composite potential  $ae^{-\kappa_r r}/r + l_B/r$  (light red dashed line). The inset displays the same set of curves as the main diagram, yet for an anion-cation pair, where the Coulomb potential  $-l_B/r$  is attractive.

#### A. Specific case $a = b = c$

We aim to compute the two potentials  $\Psi_e(x)$  and  $\Psi_h(x)$ . They solve the Poisson-Fermi and screened Poisson-Fermi equations [see Eqs. (25)], which for  $a = b = c$  and  $\alpha = \gamma = 0$  read

$$\Psi_e'' = \frac{2\phi_0}{ql^2} e^{-\eta} \sinh \Psi_e, \quad (32a)$$

$$\Psi_h'' - \kappa^2 \Psi_h = -\frac{2\phi_0}{l_h^2} \left( \frac{e^{-\eta}}{q} \cosh \Psi_e - 1 \right), \quad (32b)$$

with the factor  $q = 1 + 2\phi_0(e^{-\eta} \cosh \Psi_e - 1)$ . While the Poisson-Fermi equation (32a) is real valued, the screened Poisson-Fermi equation (32b) is complex valued. Separating its real and imaginary parts gives rise to the two equations

$$\begin{aligned} \eta'' - (\kappa_r^2 - \kappa_c^2)\eta + 2\kappa_r\kappa_c\tau &= -\frac{2\phi_0}{l_h^2} \left( \frac{e^{-\eta}}{q} \cosh \Psi_e - 1 \right), \\ \tau'' - (\kappa_r^2 - \kappa_c^2)\tau - 2\kappa_r\kappa_c\eta &= 0, \end{aligned} \quad (33)$$

whose solution defines the complex-valued potential  $\Psi_h(x) = \eta(x) + i\tau(x)$ .

Next we discuss the boundary conditions for Eqs. (32). Recall that Eqs. (26) specify the boundary condition at the macroion surfaces for the degenerate case. For our system of planar symmetry (see Fig. 2), together with  $\theta_h = 0$ , these give

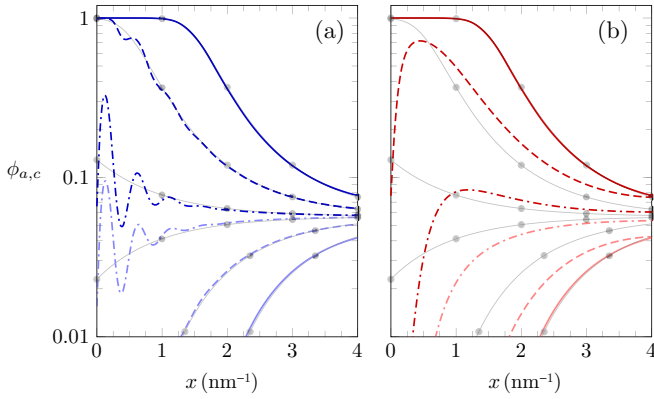


FIG. 4. Local volume fractions of anions  $\phi_a$  (dark blue in the left and dark red in the right diagram) and cations  $\phi_c$  (light blue in the left and light red in the right diagram) as a function of  $x$  for three surface charge densities:  $\sigma_e = 2 e \text{ nm}^{-2}$  (solid lines),  $\sigma_e = 1 e \text{ nm}^{-2}$  (dashed lines), and  $\sigma_e = 0.1 e \text{ nm}^{-2}$  (dash-dotted lines). Corresponding gray lines (added gray bullets facilitate recognition of overlapping curves) mark the complete absence of hydration interactions ( $a = 0$ ). Diagrams refer to the (a) presence ( $\kappa_c = 12.5 \text{ nm}^{-1}$ ) and (b) absence ( $\kappa_c = 0$ ) of the oscillatory component in the hydration potential. All curves are derived for  $d \rightarrow \infty$  and  $\nu = 1 \text{ nm}^3$ . Note the logarithmic scale of the ordinate.

rise to

$$\Psi_e'(0) = -\frac{\nu}{l^2} \frac{\sigma_e}{e}, \quad (34a)$$

$$\Psi_h'(0) - \kappa \Psi_h(0) = -\frac{\nu}{l_h^2} \sigma_h. \quad (34b)$$

Note that Eqs. (34) assume that the macroions are sufficiently thick so that the hydration potential decays to zero somewhere inside the macroions. This allows us to integrate the equation  $\Psi_h''(x) = \kappa^2 \Psi_h(x)$  inside each of the two macroions, leading to Eqs. (34). The boundary condition for the hydration potential  $\Psi_h$  in Eq. (34b) is complex valued. When separating real and imaginary parts we find

$$\begin{aligned} \eta'(0) - \kappa_r \eta(0) + \kappa_c \tau(0) &= -\frac{\nu}{l_h^2} \sigma_h, \\ \tau'(0) - \kappa_r \tau(0) - \kappa_c \eta(0) &= 0. \end{aligned} \quad (35)$$

The symmetry relations  $\Psi_e(x) = \Psi_e(d-x)$  and  $\Psi_h(x) = \Psi_h(d-x)$  entail the two additional boundary conditions  $\Psi_e'(d/2) = \Psi_h'(d/2) = 0$ .

Before analyzing the differential capacitance and pressure, we find it useful to present numerical results of the local volume fractions  $\phi_a(x)$  and  $\phi_c(x)$  for a few specific examples. To this end, we focus on a single isolated surface ( $d \rightarrow \infty$ ) and microions of volume  $\nu = 1 \text{ nm}^3$ . Note that the latter choice implies a bulk volume fraction  $\phi_0 = 0.057$  of the anions and cations. Figure 4 shows  $\phi_a(x)$  [dark blue in Fig. 4(a) and dark red in Fig. 4(b)] and  $\phi_c(x)$  [light blue in Fig. 4(a) and light red in Fig. 4(b)] for three surface charge densities:  $\sigma_e = 2 e \text{ nm}^{-2}$  (solid lines),  $\sigma_e = 1 e \text{ nm}^{-2}$  (dashed lines), and  $\sigma_e = 0.1 e \text{ nm}^{-2}$  (dash-dotted lines). Corresponding gray lines mark the complete absence of hydration interactions ( $a = 0$ ). In this case, our model reduces to classical lattice gas mean-field electrostatics [25]. Figures 4(a) and 4(b) re-

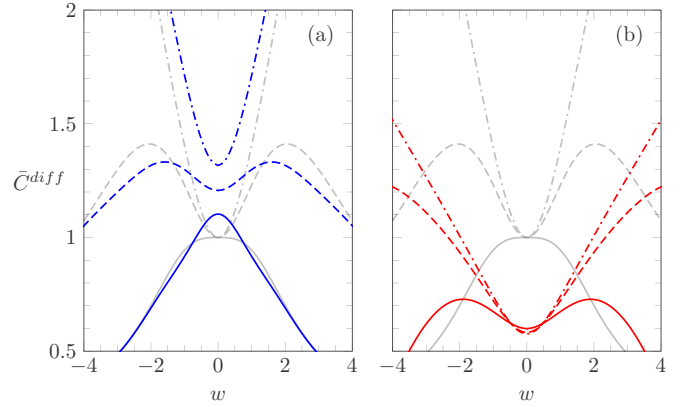


FIG. 5. Scaled differential capacitance  $\bar{C}^{\text{diff}}$  as a function of the scaled surface charge density  $w = 2\pi l_B l_D \sigma_e / e$  (a) in the presence of the oscillating Yukawa potential ( $\kappa_c = 12.5 \text{ nm}^{-1}$ , blue lines), (b) in the presence of the nonoscillating Yukawa potential ( $\kappa_c = 0$ , red lines), and (a) and (b) in the absence of hydration-mediated interactions ( $a = 0$ , gray lines). Solid, dashed, and dash-dotted lines are calculated for ion volumes  $\nu = 3, 1, \text{ and } 0.1 \text{ nm}^3$ , respectively.

fer, respectively, to the presence ( $\kappa_c = 12.5 \text{ nm}^{-1}$ ) and absence ( $\kappa_c = 0$ ) of the oscillatory component in the hydration potential.

We first discuss the presence of the oscillatory component in the Yukawa potential [Fig. 4(a)]. For small  $\sigma_e$ , we observe additional damped oscillations of  $\phi_a$  and  $\phi_c$  when compared to the classical lattice gas prediction, where hydration interactions are absent ( $a = 0$ ). The oscillations are caused mainly by the hydration-mediated ion-surface interactions and they are in phase because the hydration potential is the same irrespective of the ion type. We note that the limit of small  $\sigma_e$  renders the ion size irrelevant, as it does in classical Poisson-Boltzmann theory. For large  $\sigma_e$ , steric and electrostatic interactions dominate: The anions close to the surface are densely packed and hydration interactions become irrelevant. Hence the cases  $a = 1 \text{ nm}$  (solid blue and solid red curves) and  $a = 0$  (corresponding gray curves) coincide. The observed counterion saturation for large  $\sigma_e$  arises because we have incorporated the lattice gas mixing entropy in Eq. (13) (instead of an ideal gas mixing entropy) into our mean-field model [25]. Next we discuss the absence of the oscillatory component in the Yukawa potential [Fig. 4(b)]. The strictly repulsive nature of the Yukawa potential can then lead to a pronounced depletion zone of the ions close to the electrode, which is reminiscent of a Stern layer [54,58,59]. It does so for small  $\sigma_e$ , whereas for large  $\sigma_e$  the strong electrostatic ion-surface interactions again render the hydration interactions irrelevant.

Next we investigate how the scaled differential capacitance  $\bar{C}^{\text{diff}} = l_D C^{\text{diff}} / \epsilon_w \epsilon_0$  of a single planar electrode (that is,  $d \rightarrow \infty$ ) is influenced by the Yukawa potential. Figure 5 displays  $\bar{C}^{\text{diff}}$  as a function of the scaled (dimensionless) electrode surface charge density  $w = 2\pi l_B l_D \sigma_e / e$  in the presence of oscillating [ $\kappa_c = 12.5 \text{ nm}^{-1}$ , blue lines in Fig. 5(a)] and nonoscillating [ $\kappa_c = 0$ , red lines in Fig. 5(b)] Yukawa potentials. Solid, dashed, and dash-dotted lines are calculated for ion volumes  $\nu = 3, 1, \text{ and } 0.1 \text{ nm}^3$ , respectively. Gray lines

in both diagrams mark the absence of hydration-mediated interactions ( $a = 0$ ). Recall that these lines are described by the lattice gas result in Eq. (29), which predicts the transition from camel-shaped (for  $\phi_0 < 1/6$ ) to bell-shaped (for  $\phi_0 > 1/6$ ) profiles. Indeed,  $\phi_0 = 1/6$  corresponds to an ion volume of  $v = \phi_0/n_0 = 1/(6 \times 0.057) \text{ nm}^3 = 2.92 \text{ nm}^3$  that separates bell-shaped profiles (for  $v = 3 \text{ nm}^3$  in Fig. 5) from camel-shape profiles (for  $v = 1$  and  $0.1 \text{ nm}^3$  in Fig. 5). Adding our oscillating [blue lines in Fig. 5(a)] or nonoscillating Yukawa potential [red lines in Fig. 5(b)] does shift but does not eliminate the presence of a camel-to-bell shape transition when  $v$  increases [in Fig. 5(b) it occurs for  $v > 3 \text{ nm}^3$ ]. It does however modify the magnitude of  $C^{\text{diff}}$ , especially for small  $|\sigma_e|$ . In particular, at  $\sigma_e = 0$  we observe  $C^{\text{diff}}$  to be increased ( $\bar{C}^{\text{diff}} > 1$ ) for the oscillating Yukawa potential and decreased ( $\bar{C}^{\text{diff}} < 1$ ) for the nonoscillating Yukawa potential. The increase in the former case is a result of the local minimum of the oscillating Yukawa potential near  $r = 0.2 \text{ nm}$  (see Fig. 3), leading to an accumulation of counterions near the electrode (see Fig. 4). The decrease in the latter case reflects ion depletion near the electrode due to the repulsive nature of the nonoscillating Yukawa potential. We also note that  $C^{\text{diff}}$  decreases with  $v$  at  $\sigma_e = 0$  for the oscillating Yukawa potential and increases (to a very minor extent) with  $v$  at  $\sigma_e = 0$  for the nonoscillating Yukawa potential. The tendency in both cases to approach the result for the absence of hydration interactions  $\bar{C}^{\text{diff}} = 1$  for growing  $v$  originates in the diminished importance of the Yukawa potential for larger ions. Recall from Eqs. (1) that the Yukawa potentials are measured center to center between the ions. No computer simulations have been performed so far for solvent-mediated oscillating Yukawa potentials that are present in addition to the bare Coulomb potential. For the nonoscillating Yukawa potential, however, recent Monte Carlo simulations qualitatively agree with the behavior in Fig. 5(b) [54,59,60]. The small increase of  $\bar{C}^{\text{diff}}$  with  $v$  at  $\sigma_e = 0$  is opposite of what the Stern layer model predicts and has been interpreted in terms of the larger osmotic pressure exerted by the larger ions, which pushes them closer to the electrode surface [54,59,60].

We finally investigate the pressure  $P$  that acts between the two planar macroions (see Fig. 2) as a function of their separation  $d$ . In the limiting case that both macroion surfaces are uncharged and no salt is present in the solution ( $\sigma_e = 0$  and  $\phi_0 = 0$ ), the two macroions still exert a pressure onto each other due to their ability to produce hydration fields. The hydration potential then satisfies  $\Psi_h'' = \kappa^2 \Psi_h$ , with the two boundary conditions  $\Psi_h'(0) - \kappa \Psi_h(0) = -v\sigma_h/l_h^2$  and  $\Psi_h'(d/2) = 0$ . This is solved by

$$\Psi_h(x) = \frac{v\sigma_h}{2l_h^2\kappa} e^{-\kappa(d/2)} \cosh\left[\kappa\left(\frac{d}{2} - x\right)\right]. \quad (36)$$

The pressure can then be calculated from Eq. (31); at position  $d/2$ , we obtain

$$\frac{Pv}{k_B T} = \frac{1}{2} \left(\frac{v\sigma_h}{l_h}\right)^2 e^{-\kappa_c d} \cos(\kappa_c d). \quad (37)$$

Note that we can calculate the pressure in Eq. (37) also directly from integrating the hydration-mediated interactions

between the two surfaces

$$\begin{aligned} \frac{Pv}{k_B T} &= -\frac{1}{2} \left(\frac{v\sigma_h}{l_h}\right)^2 \\ &\times \frac{d}{dd} \int_0^\infty dr r \frac{e^{-\kappa_r \sqrt{d^2+r^2}}}{\sqrt{d^2+r^2}} \cos(-\kappa_c \sqrt{d^2+r^2}) \\ &= \frac{1}{2} \left(\frac{v\sigma_h}{l_h}\right)^2 e^{-\kappa_c d} \cos(\kappa_c d), \end{aligned} \quad (38)$$

where  $d/dd$  denotes the first derivative with respect to the separation  $d$  between the two macroion surfaces. We point out that the oscillating, exponentially decaying hydration pressure is in qualitative agreement with experimental [62] and computational [63–65] results.

Another limiting case is that of small  $\sigma_e$  and  $\sigma_h$ . Here the potentials  $\Psi_e(x)$  and  $\Psi_h(x)$  deviate only slightly from the solution  $\Psi_e(x) = \Psi_h(x) = 0$  that we obtain for  $\sigma_e = \sigma_h = 0$ . Hence, we can linearize Eqs. (32), leading to the two decoupled equations  $l^2 \Psi_e'' = 2\phi_0 \Psi_e$  and  $l_h^2 (\Psi_h'' - \kappa^2 \Psi_h) = -2\phi_0(2\phi_0 - 1)\Psi_h$ , to be solved subject to the boundary conditions  $l^2 \Psi_e'(0) = -v\sigma_e/e$ ,  $\Psi_h'(0) - \kappa \Psi_h(0) = -v\sigma_h/l_h^2$ , and  $\Psi_e'(d/2) = \Psi_h'(d/2) = 0$ . At position  $d/2$ , we find, for the two potentials,

$$\begin{aligned} \Psi_e\left(\frac{d}{2}\right) &= \frac{v\sigma_e}{l^2 e} \frac{l_D}{\sinh\left(\frac{d}{2l_D}\right)}, \\ \Psi_h\left(\frac{d}{2}\right) &= \frac{v\sigma_h}{l_h^2} \frac{1}{\kappa \cosh\left(\frac{d}{2}\tilde{\kappa}\right) + \tilde{\kappa} \sinh\left(\frac{d}{2}\tilde{\kappa}\right)}, \end{aligned} \quad (39)$$

where we have defined the complex-valued inverse length  $\tilde{\kappa}$  through  $\tilde{\kappa}^2 = \kappa^2 + 2\phi_0(1 - 2\phi_0)/l_h^2$  and where we recall the Debye screening length  $l_D = l/\sqrt{2\phi_0}$  with  $l^2 = v/4\pi l_B$ . Equations (39) can be used to calculate the pressure

$$\begin{aligned} \frac{Pv}{k_B T} &= \phi_0 \Psi_e^2\left(\frac{d}{2}\right) + \frac{l_h^2}{2} \left(\frac{1}{2}\right) \left[ \tilde{\kappa}^2 \Psi_h^2\left(\frac{d}{2}\right) + \text{c.c.} \right] \\ &= \frac{1}{2} \left(\frac{v\sigma_e}{le}\right)^2 \frac{1}{\left[\sinh\left(\frac{d}{2l_D}\right)\right]^2} \\ &\quad + \frac{1}{2} \left(\frac{v\sigma_h}{l_h}\right)^2 \frac{1}{2} \left\{ \frac{1}{\left[\sinh\left(\frac{d}{2}\tilde{\kappa}\right) + \frac{\kappa}{\tilde{\kappa}} \cosh\left(\frac{d}{2}\tilde{\kappa}\right)\right]^2} + \text{c.c.} \right\}. \end{aligned} \quad (40)$$

In the limit  $\sigma_e = 0$  and  $\phi_0 = 0$  we obtain  $\tilde{\kappa} = \kappa$  and Eq. (40) recovers Eq. (37). Furthermore, because electrostatic and hydration contributions decouple in the linear limit, we find for the scaled differential capacitance of an isolated, uncharged planar surface simply  $\bar{C}^{\text{diff}} = 1$ . This is the same result as for the classical Poisson-Boltzmann model in the limit of a vanishing surface charge density  $\sigma_e$ . Hence, hydration interactions do not affect the differential capacitance in the limit of sufficiently small  $\sigma_e$  and  $\sigma_h$ .

Figure 6 presents the (scaled) pressure  $Pv/k_B T$  as a function of the separation  $d$  between the two macroions for  $\sigma_e = -0.5 e \text{ nm}^{-2}$  [Fig. 6(a)] and  $\sigma_e = -0.75 e \text{ nm}^{-2}$  [Fig. 6(b)]. Results for the oscillating Yukawa potential ( $\kappa_c = 12.5 \text{ nm}^{-1}$ ) are shown in blue and those for the nonoscillating Yukawa potential ( $\kappa_c = 0$ ) in red. We have added the prediction of

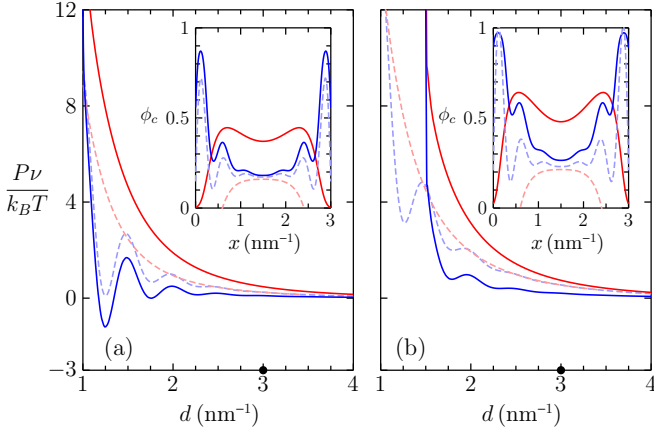


FIG. 6. Scaled pressure  $P\nu/k_B T$  as a function of the separation  $d$  between the two planar macroion surfaces for (a)  $\sigma_e = -0.5 e \text{ nm}^{-2}$  and (b)  $\sigma_e = -0.75 e \text{ nm}^{-2}$ . Results for the oscillating Yukawa potential ( $\kappa_c = 12.5 \text{ nm}^{-1}$ ) are shown in blue [with the light blue dashed line for the linear model according to Eq. (40)] and those for the nonoscillating Yukawa potential ( $\kappa_c = 0$ ) in red [with the light red dashed line for the linear model according to Eq. (40)]. Insets show the counterion volume fraction  $\phi_c$  as a function of location  $x$  between the macroions, with  $d = 3 \text{ nm}$  (marked by a black bullet in the main diagram). All curves are calculated for an ion volume  $\nu = 1 \text{ nm}^3$ .

the linearized theory according to Eq. (40) (blue dashed line for the oscillating Yukawa potential and red dashed line for the nonoscillating Yukawa potential). The two insets display the local cation concentration  $\phi_c(x)$  for a separation  $d = 3 \text{ nm}$  between the two macroions. Here too solid and dashed lines refer to the full nonlinear and to the linearized models, respectively.

Figure 6 demonstrates that the presence of the oscillatory Yukawa potential leads to oscillations of the pressure  $P$ , whereas the presence of the strictly repulsive, nonoscillating Yukawa potential does not. Oscillations may lead to a negative pressure and thus attractive interactions between the two like-charged macroion surfaces for certain ranges of  $d$ . Increasing the surface charge density  $\sigma_e$  strengthens the repulsive component of  $P$  and may thus turn an initially attractive interaction into a repulsion. This is indeed the case in Fig. 6, where the pressure can be negative for  $\sigma_e = -0.5 e \text{ nm}^{-2}$  but always remains positive for  $\sigma_e = -0.75 e \text{ nm}^{-2}$ . We note that the prediction for  $P$  according to the linearized model, as described by Eq. (40), is still reasonably close to that of the full nonlinear model for  $\sigma_e = -0.5 e \text{ nm}^{-2}$ , but increasingly fails as  $|\sigma_e|$  is increased. In addition, the linearized model is more accurate for the oscillating Yukawa potential as compared to the nonoscillating one. This is a consequence of  $|\cos(\kappa_c r)| \leq 1$  for the oscillatory component of the Yukawa potential, which always reduces the impact of the hydration-mediated interactions and thus the magnitudes of the potentials  $\Psi_e(x)$  and  $\Psi_h(x)$ . Note finally that the pressure  $P$  for the full (nonlinear) model diverges at  $d = 1 \text{ nm}$  for  $\sigma_e = -0.5 e \text{ nm}^{-2}$  and at  $d = 1.5 \text{ nm}$  for  $\sigma_e = -0.75 e \text{ nm}^{-2}$ . Counterions are densely packed between the two macroion surfaces at  $d = 2|\sigma_e|/e\nu$ , thus preventing any further approach of the two macroions.

The linearized model does not account for these ion packing considerations.

### B. Specific case $a = -b = c$

Here the hydration-mediated interaction between anion-cation pairs is attractive, equal in magnitude, and opposite in sign to the repulsion between anion-anion and between cation-cation pairs. In the following, we repeat all calculations carried out in the preceding section, which will allow us to assess the implications of switching the sign of  $b$ . For  $a = -b = c$  and  $\alpha = \gamma = 0$ , the two potentials  $\Psi_e(x)$  and  $\Psi_h(x)$  satisfy the Poisson-Fermi and screened Poisson-Fermi equations [see Eqs. (25)]

$$\begin{aligned} \Psi_e'' &= \frac{2\phi_0}{ql^2} \sinh(\Psi_e - \eta), \\ \Psi_h'' - \kappa^2 \Psi_h &= -\frac{2\phi_0}{ql_h^2} \sinh(\Psi_e - \eta), \end{aligned} \quad (41)$$

with the factor  $q = 1 + 2\phi_0[\cosh(\Psi_e - \eta) - 1]$ . Here again the screened Poisson-Fermi equation is complex valued, with  $\kappa = \kappa_r + i\kappa_c$  and  $\Psi_h(x) = \eta(x) + i\tau(x)$ ; its real and imaginary parts can be separated analogously to Eqs. (33). The boundary conditions for the case  $a = -b = c$  are the same as for  $a = b = c$ , given by  $\Psi_e'(d/2) = \Psi_h'(d/2) = 0$  and Eqs. 34 [or, equivalently, Eqs. (35) when separating real and imaginary parts]. As stated above, we use the value  $\sigma_h = 5 \text{ nm}^{-2}$  everywhere in this work. With this choice, however, we no longer obtain solutions for  $\Psi_e(x)$  and  $\Psi_h(x)$  that are invariant upon inverting the sign of  $\sigma_e$ . The reason for this loss of symmetry is the appearance of a minus sign in the expression for  $\sigma_h$  according to Eq. (27), that is,  $\sigma_h = \sigma_a - \sigma_c$  for our present case of  $a = -b = c$ . Preserving the invariance of  $\Psi_e(x)$  and  $\Psi_h(x)$  upon inverting the sign of  $\sigma_e$  would require us to choose  $\sigma_a = \sigma_c$  and thus  $\sigma_h = 0$ . To obtain  $\sigma_h = 5 \text{ nm}^{-2}$ , we may, for example, choose  $\sigma_a = 2.5 \text{ nm}^{-2}$  and  $\sigma_c = -2.5 \text{ nm}^{-2}$ . Obviously then, with different cation-surface and anion-surface interactions, the system is no longer symmetric with respect to changing the sign of  $\sigma_e$ .

As in the preceding section, we first focus on the local volume fractions  $\phi_a(x)$  and  $\phi_c(x)$  in the vicinity of a single isolated electrode ( $d \rightarrow \infty$ ) and ions of volume  $\nu = 1 \text{ nm}^3$ . Figure 7 shows  $\phi_a(x)$  [dark blue in Figs. 7(a) and 7(c) and dark red in Figs. 7(b) and 7(d)] and  $\phi_c(x)$  [light blue in Figs. 7(a) and 7(c) and light red in Figs. 7(b) and 7(d)] for the surface charge densities:  $\sigma_e = \pm 2 e \text{ nm}^{-2}$  (solid lines),  $\sigma_e = \pm 1 e \text{ nm}^{-2}$  (dashed lines), and  $\pm \sigma_e = 0.1 e \text{ nm}^{-2}$  (dash-dotted lines). Results for the three positive and negative  $\sigma_e$  are displayed in Figs. 7(a) and 7(b) and Figs. 7(c) and 7(d), respectively. Figures 7(a) and 7(c) and Figs. 7(b) and 7(d) refer to the presence ( $\kappa_c = 12.5 \text{ nm}^{-1}$ ) and absence ( $\kappa_c = 0$ ) of the oscillatory component in the hydration potential, respectively. Gray lines in all four diagrams mark the absence of hydration-mediated interactions ( $a = 0$ ).

We first discuss Figs. 7(a) and 7(c), where the oscillatory component in the hydration potential is present. As in Fig. 4, oscillations in the volume fractions of the ions are present for small  $|\sigma_e|$  but not for large  $|\sigma_e|$ . High surface charge densities lead to dense ion packing, which renders hydration-mediated

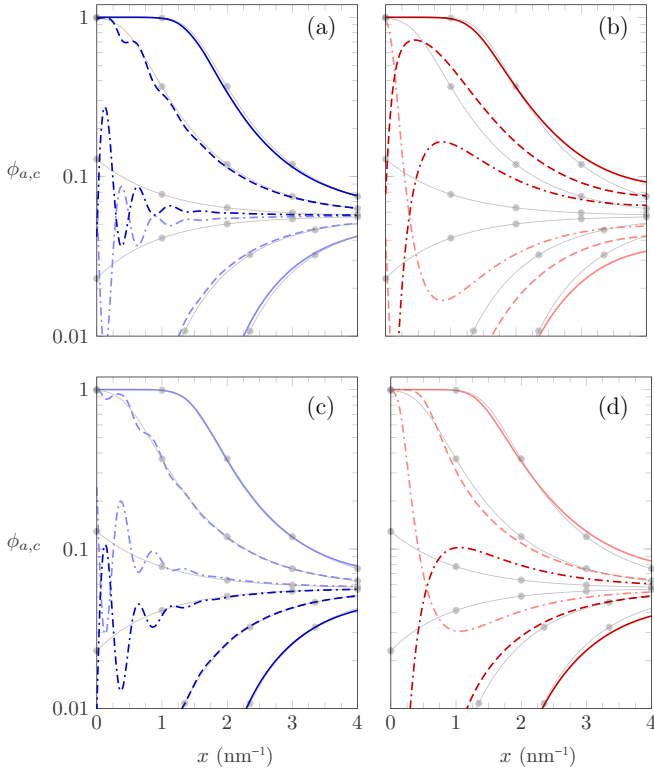


FIG. 7. Local volume fractions of anions  $\phi_a$  [dark blue in (a) and (c) and dark red in (b) and (d)] and cations  $\phi_c$  [light blue in (a) and (c) and light red in (b) and (d)] as a function of  $x$  for the surface charge densities:  $\sigma_e = \pm 2 e \text{ nm}^{-2}$  (solid lines),  $\sigma_e = \pm 1 e \text{ nm}^{-2}$  (dashed lines), and  $\sigma_e = \pm 0.1 e \text{ nm}^{-2}$  (dash-dotted lines). Results are shown for (a) and (b)  $\sigma_e > 0$  and (c) and (d)  $\sigma_e < 0$ . Corresponding gray lines in all four diagrams (added gray bullets facilitate recognition of overlapping curves) mark the complete absence of hydration interactions ( $a = 0$ ). Diagrams refer to the (a) and (c) presence ( $\kappa_c = 12.5 \text{ nm}^{-1}$ ) and (b) and (d) absence ( $\kappa_c = 0$ ) of the oscillatory component in the hydration potential. All curves are derived for  $d \rightarrow \infty$  and  $\nu = 1 \text{ nm}^3$ . Note the logarithmic scale of the ordinate.

interactions irrelevant. For small surface charge densities we observe spatial oscillations that are phase shifted so that a local maximum volume fraction of one ion type corresponds to a minimum of the other ion type. This can lead to ion layering, that is, one or several layers of ions with alternating sign. The origin of the layering lies in the preferential hydration interactions of cations as compared to the anions with the electrode surface. Comparing the corresponding lines in Figs. 7(a) and 7(c) reveals the differences in the ion distributions that result from inverting the sign of  $\sigma_e$ : The lack of symmetry is most visible for the dash-dotted lines (small  $|\sigma_e|$ ), where hydration-mediated ion-surface interactions dominate. Next we discuss Figs. 7(b) and 7(d), where no oscillatory component is present in the hydration potential. Here we observe a pronounced influence of the preferential hydration-mediated interaction of the surface with cations over that with anions. Cations are attracted to the surface and anions are repelled; when  $|\sigma_e|$  is small this leads to similar ion distributions even when the sign of  $\sigma_e$  is inverted (compare the dark red and light red dash-dotted lines in Fig. 7). Even at larger  $|\sigma_e|$

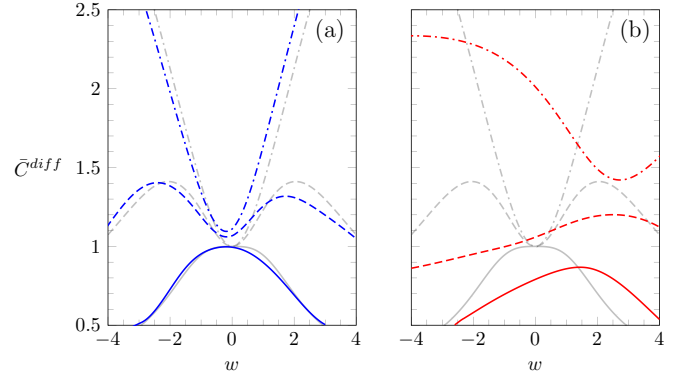


FIG. 8. Scaled differential capacitance  $\bar{C}^{\text{diff}}$  as a function of the scaled surface charge density  $w = 2\pi l_B l_D \sigma_e / e$  (a) in the presence of the oscillating Yukawa potential ( $\kappa_c = 12.5 \text{ nm}^{-1}$ , blue lines), (b) in the presence of the nonoscillating Yukawa potential ( $\kappa_c = 0$ , red lines), and (a) and (b) in the absence of hydration-mediated interactions ( $a = 0$ , gray lines). Solid, dashed, and dash-dotted lines are calculated for ion volumes  $\nu = 3, 1$ , and  $0.1 \text{ nm}^3$ , respectively.

(compare the dark red and light red dashed lines in Fig. 7) the hydration-mediated anion depletion and cation accumulation are evident. Only at very large  $|\sigma_e|$  do the electrostatic ion-surface interactions dominate over the hydration-mediated ones (compare the dark red and light red solid lines in Fig. 7).

Next we investigate the scaled differential capacitance  $\bar{C}^{\text{diff}}$  of a single planar electrode ( $d \rightarrow \infty$ ), which is displayed in Fig. 8 as a function of the scaled (dimensionless) electrode surface charge density  $w = 2\pi l_B l_D \sigma_e / e$  in the presence of oscillating [ $\kappa_c = 12.5 \text{ nm}^{-1}$ , blue lines in Fig. 8(a)] and nonoscillating [ $\kappa_c = 0$ , red lines in Fig. 8(b)] Yukawa potentials. As in Fig. 5, we show solid, dashed, and dash-dotted lines that are calculated for ion volumes  $\nu = 3, 1$ , and  $0.1 \text{ nm}^3$ , respectively. Gray lines in both diagrams mark the absence of hydration-mediated interactions ( $a = 0$ ). An immediately apparent feature of Fig. 8 is the asymmetry of  $\bar{C}^{\text{diff}}$  with respect to inverting the sign of  $\sigma_e$ . When the oscillatory component of the Yukawa potential is present [Fig. 8(a)], the hydration-mediated interactions exert only a very minor influence on  $\bar{C}^{\text{diff}}$ . When the oscillatory component is absent [Fig. 8(b)], the modifications are substantial. To rationalize them, we recall that according to  $\sigma_h = 5 \text{ nm}^{-2}$  the electrode effectively attracts cations and repels anions through hydration-mediated interactions. At some positive charge density  $\sigma_e > 0$ , electrostatic anion attraction and hydration-mediated anion repulsion will balance each other, shifting the extremal points (maximum or minimum) of the  $\bar{C}^{\text{diff}}$  curves toward positive  $\sigma_e$ . We observe this shift to be smaller for larger ions because growing  $\nu$  renders hydration-mediated interactions less pronounced. When inverting the sign of  $b$  from positive to negative [compare Figs. 5(b) and 8(b)],  $\bar{C}^{\text{diff}}$  tends to grow because the reversal of the anion-cation repulsion into an attraction leads to a more condensed electric double layer. Note that the transition from camel-shaped to bell-shaped profiles remains virtually unaffected in the presence of the oscillatory component of the Yukawa potential but is shifted to smaller  $\nu$  in its absence. Both in the presence and in the absence of the oscillatory component of the Yukawa potential, increasing the ion size reduces  $\bar{C}^{\text{diff}}$ .

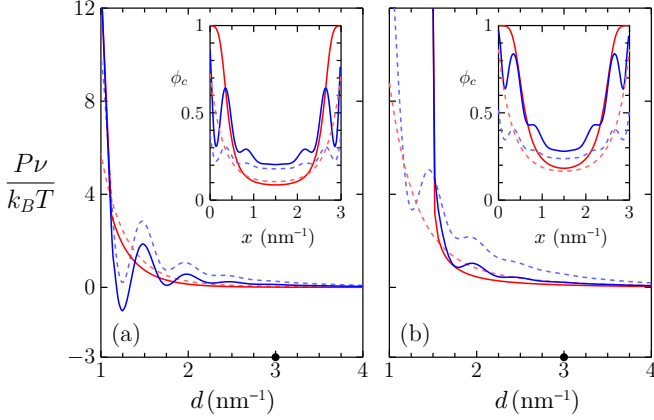


FIG. 9. Scaled pressure  $P\nu/k_B T$  as a function of the separation  $d$  between the two planar macroion surfaces for (a)  $\sigma_e = -0.5 e \text{ nm}^{-2}$  and (b)  $\sigma_e = -0.75 e \text{ nm}^{-2}$ . Results for the oscillating Yukawa potential ( $\kappa_c = 12.5 \text{ nm}^{-1}$ ) are shown in blue and those for the nonoscillating Yukawa potential ( $\kappa_c = 0$ ) in red. Insets show the counterion volume fraction  $\phi_c$  as a function of location  $x$  between the macroions, with  $d = 3 \text{ nm}$  (marked by a black bullet in the main diagram). Dashed lines in main diagram and inset refer to the linearized model. All curves are calculated for an ion volume  $\nu = 1 \text{ nm}^3$ .

Recall from the discussion following Eq. (40) that for  $a = b = c$  the differential capacitance remains unaffected by hydration-mediated interactions in the linearized theory, where both  $\sigma_h$  and  $\sigma_e$  are sufficiently small. For  $a = -b = c$ , we obtain from Eqs. (41) the two linearized equations  $l^2 \Psi_e'' = 2\phi_0(\Psi_e - \eta)$  and  $l_h^2(\Psi_h'' - \kappa^2 \Psi_h) = -2\phi_0(\Psi_e - \eta)$ , which are now coupled. Analytic solutions for the differential capacitance (and similarly for the pressure) are cumbersome. Only for the case of the nonoscillating Yukawa potential ( $\kappa_c = 0$ ) can we extract a simple analytic result for the differential capacitance of an isolated planar electrode,

$$C^{\text{diff}} = \frac{\epsilon_w \epsilon_0}{\frac{1}{\omega_1} + \frac{1}{\omega_2} - \frac{1}{l_D \omega_1 \omega_2}}, \quad (42)$$

where  $\omega_1$  and  $\omega_2$  are the two positive roots of the equation

$$\omega^4 - \left( \frac{1}{l_D^2} + \kappa_r^2 + \frac{2\phi_0}{l_h^2} \right) \omega^2 + \frac{\kappa_r^2}{l_D^2} = 0. \quad (43)$$

Switching off hydration-mediated interactions by setting  $a = 0$  implies that  $l_h^2 = \nu/4\pi a \rightarrow \infty$  and thus  $\omega_1 = \kappa_r$  and  $\omega_2 = 1/l_D$ . This then indeed recovers the classical Poisson-Boltzmann prediction  $C^{\text{diff}} = \epsilon_w \epsilon_0 / l_D$  (or, equivalently,  $\bar{C}^{\text{diff}} = 1$ ) in the limit of a vanishing surface charge density  $\sigma_e$ .

Figure 9 presents the (scaled) pressure  $P\nu/k_B T$  as a function of the separation  $d$  between two planar macroion surfaces for  $\sigma_e = -0.5 e \text{ nm}^{-2}$  [Fig. 9(a)] and  $\sigma_e = -0.75 e \text{ nm}^{-2}$  [Fig. 9(b)]. As in Fig. 6, results for the oscillating Yukawa potential ( $\kappa_c = 12.5 \text{ nm}^{-1}$ ) are shown in blue and those for the nonoscillating Yukawa potential ( $\kappa_c = 0$ ) in red. The two insets display the local cation concentration  $\phi_c(x)$  for a separation  $d = 3 \text{ nm}$  between the two macroions. Dashed lines in the main diagram and inset refer to the linearized model. Note that the sole difference in Figs. 6 and 9 is the sign of  $b$ . As already

observed for the differential capacitance, switching the sign of  $b$  from positive to negative has only moderate consequences when the oscillatory component of the Yukawa potential is present ( $\kappa_c = 12.5 \text{ nm}^{-1}$ ) but drastically reduces the pressure for  $\kappa_c = 0$ . An especially notable difference in the latter case is the maximal cation volume fraction  $\phi_c$  close to the two macroions for  $b < 0$ , whereas for  $b > 0$  we recall from Fig. 4 that cations were depleted from the vicinity of the two macroions. The reason for these differences is of course that our choice  $\sigma_h = 5 \text{ nm}^{-2}$  implies preferential cation-macroion attraction for  $b < 0$ , whereas for  $b > 0$  all ions are repelled from the macroion surfaces (see also our discussion of Fig. 7 above). Despite the differences, Figs. 6 and 9 both predict that increasing  $\sigma_e$  changes the interaction between the macroions from being attractive to being repulsive.

#### IV. CONCLUSION

The main goal of this work was to develop a mean-field model for microions and macroions that interact with each other through composite Coulomb and oscillating Yukawa potentials. The oscillating Yukawa potentials serve as simple representations for ion-specific hydration-mediated interactions in aqueous solutions. The oscillating nature of the Yukawa potentials is supported by experimental and computational evidence. Ion specificity arises by equipping anion-anion, anion-cation, and cation-cation pairs each with their own interaction strength and phase shift. The interaction of anions and cations with macroion surfaces is also ion specific, with individual interaction strengths and phase shifts. Our model is comprehensive in the sense that it covers all cases, nondegenerate and degenerate (recall that the latter case is characterized by a singular interaction matrix  $\mathcal{A}_h$ ). We have used a lattice gas model to account for the ion size in the most approximate manner.

We exemplify our general model by calculating the differential capacitance of a single planar electrode and the pressure between two interacting planar macroions. Our examples are based on a few specific sets of parameters: They illustrate rather than comprehensively analyze the predictions of our theoretical model. Among those are the asymmetric shapes of the differential capacitance due to ion-specific effects as well as the attraction between like-charged macroions and its regulation through the macroion surface charge density. Future work may attempt to employ the present model to rationalize experimental data. Perhaps more important would be to address the approximations that are still present in our work, especially the assumption of a uniform dielectric constant and the modeling of the ion entropy through a lattice gas.

#### ACKNOWLEDGMENTS

J.S. thanks North Dakota Space Grant Consortium for an undergraduate fellowship. G.V.B. is grateful to the São Paulo Research Foundation (FAPESP) for support through a postdoctoral scholarships, Grant No. 2017/21772-2. S.J.d.C. thanks the São Paulo Research Foundation (FAPESP), Grant No. 2018/01841-2. S.M. thanks ND EPSCoR for support. We acknowledge discussions with Bjorn Berntson and Klemen Bohinc.

- [1] B. Maier and J. O. Rädler, *Macromolecules* **33**, 7185 (2000).
- [2] A. Mulgrew-Nesbitt, K. Diraviyam, J. Wang, S. Singh, P. Murray, Z. Li, L. Rogers, N. Mirkovic, and D. Murray, *Biochim. Biophys. Acta Mol. Cell Biol. Lipids* **1761**, 812 (2006).
- [3] V. P. Zhdanov and B. Kasemo, *Biophys. Chem.* **146**, 60 (2010).
- [4] R. A. Hartvig, M. van de Weert, J. Østergaard, L. Jorgensen, and H. Jensen, *Langmuir* **27**, 2634 (2011).
- [5] F. J. Montes Ruiz-Cabello, G. Trefalt, T. Oncsik, I. Szilagyi, P. Maroni, and M. Borkovec, *J. Chem. Phys. B* **119**, 8184 (2015).
- [6] T. Oncsik, G. Trefalt, M. Borkovec, and I. Szilagyi, *Langmuir* **31**, 3799 (2015).
- [7] S. Porada, R. Zhao, A. van der Wal, V. Presser, and P. M. Biesheuvel, *Prog. Mater. Sci.* **58**, 1388 (2013).
- [8] R. Epsztein, E. Shaulsky, M. Qin, and M. Elimelech, *J. Membr. Sci.* **580**, 316 (2019).
- [9] J. R. Miller and A. F. Burke, *Electrochem. Soc. Interface* **17**, 53 (2008).
- [10] J. Yan, Q. Wang, T. Wei, and Z. Fan, *Adv. Energy Mater.* **4**, 1300816 (2013).
- [11] T. A. Ho, *Nanoscale Fluid Transport* (Springer, Berlin, 2017), pp. 37–51.
- [12] Y. Uematsu, R. R. Netz, and D. J. Bonthuis, *Langmuir* **34**, 9097 (2018).
- [13] E. J. W. Verwey and J. T. G. Overbeek, *Theory of the Stability of Lyophobic Colloids* (Elsevier, New York, 1948).
- [14] G. Gouy, *J. Phys. Theor. Appl.* **9**, 457 (1910).
- [15] D. L. Chapman, *Philos. Mag.* **25**, 475 (1913).
- [16] K. A. Sharp and B. Honig, *J. Phys. Chem.* **94**, 7684 (1990).
- [17] D. Andelman, in *Structure and Dynamics of Membranes*, 2nd ed., edited by R. Lipowsky and E. Sackmann (Elsevier, Amsterdam, 1995), Vol. 1, Sec.12, pp. 603–642.
- [18] F. Fogolari, A. Brigo, and H. Molinari, *J. Mol. Recognit.* **15**, 377 (2002).
- [19] A. Y. Grosberg, T. T. Nguyen, and B. I. Shklovskii, *Rev. Mod. Phys.* **74**, 329 (2002).
- [20] P. Grochowski and J. Trylska, *Biopolymers* **89**, 93 (2008).
- [21] M. Z. Bazant, M. S. Kilic, B. D. Storey, and A. Ajdari, *Adv. Colloid Interface Sci.* **152**, 48 (2009).
- [22] V. Vlachy, *Annu. Rev. Phys. Chem.* **50**, 145 (1999).
- [23] J.-P. Hansen and H. Löwen, *Annu. Rev. Phys. Chem.* **51**, 209 (2000).
- [24] R. Kjellander, *J. Chem. Phys.* **148**, 193701 (2018).
- [25] I. Borukhov, D. Andelman, and H. Orland, *Phys. Rev. Lett.* **79**, 435 (1997).
- [26] A. A. Kornyshev, *J. Phys. Chem. B* **111**, 5545 (2007).
- [27] L. Bhuiyan and C. Outhwaite, *J. Colloid Interface Sci.* **331**, 543 (2009).
- [28] A. Abrashkin, D. Andelman, and H. Orland, *Phys. Rev. Lett.* **99**, 077801 (2007).
- [29] P. Koehl, H. Orland, and M. Delarue, *Phys. Rev. Lett.* **102**, 087801 (2009).
- [30] M. Boström, D. R. M. Williams, and B. W. Ninham, *Phys. Rev. Lett.* **87**, 168103 (2001).
- [31] D. Ben-Yaakov, D. Andelman, D. Harries, and R. Podgornik, *J. Phys.: Condens. Matter* **21**, 424106 (2009).
- [32] D. Ben-Yaakov, D. Andelman, R. Podgornik, and D. Harries, *Curr. Opin. Colloid Interface Sci.* **16**, 542 (2011).
- [33] Y. J. Zhang and P. S. Cremer, *Annu. Rev. Phys. Chem.* **61**, 63 (2010).
- [34] W. Kunz, *Curr. Opin. Colloid Interface Sci.* **15**, 34 (2010).
- [35] J. N. Israelachvili and R. M. Pashley, *Nature (London)* **306**, 249 (1983).
- [36] J. Israelachvili and H. Wennerstrom, *Nature (London)* **379**, 219 (1996).
- [37] Y. Burak and D. Andelman, *Phys. Rev. E* **62**, 5296 (2000).
- [38] K. A. Dill, T. M. Truskett, V. Vlachy, and B. Hribar-Lee, *Annu. Rev. Biophys. Biomol. Struct.* **34**, 173 (2005).
- [39] D. Parsons, M. Bostrom, T. Maceina, A. Salis, and B. W. Ninham, *Langmuir* **26**, 3323 (2009).
- [40] D. F. Parsons, M. Boström, P. L. Nostro, and B. W. Ninham, *Phys. Chem. Chem. Phys.* **13**, 12352 (2011).
- [41] M. Kanduč, A. Schlaich, E. Schneck, and R. R. Netz, *Adv. Colloid Interface Sci.* **208**, 142 (2014).
- [42] J. I. Kilpatrick, S.-H. Loh, and S. P. Jarvis, *J. Am. Chem. Soc.* **135**, 2628 (2013).
- [43] T. Baimpos, B. R. Shrestha, S. Raman, and M. Valtiner, *Langmuir* **30**, 4322 (2014).
- [44] S. Z. Moghaddam and E. Thormann, *J. Colloid Interface Sci.* **555**, 615 (2019).
- [45] S. R. van Lin, K. K. Grotz, I. Siretanu, N. Schwierz, and F. Mugele, *Langmuir* **35**, 5737 (2019).
- [46] I. Kalcher and J. Dzubiella, *J. Chem. Phys.* **130**, 134507 (2009).
- [47] I. Kalcher, J. C. F. Schulz, and J. Dzubiella, *Phys. Rev. Lett.* **104**, 097802 (2010).
- [48] D. D. Caprio, I. Kravtsiv, T. Patsahan, and M. Holovko, *Mol. Phys.* **114**, 2500 (2016).
- [49] R. D. Coalson, A. M. Walsh, A. Duncan, and N. Ben-Tal, *J. Chem. Phys.* **102**, 4584 (1995).
- [50] J. Stafiej, D. di Caprio, and J. P. Badiali, *J. Chem. Phys.* **109**, 3607 (1998).
- [51] K. Bohinc, A. Shrestha, M. Brumen, and S. May, *Phys. Rev. E* **85**, 031130 (2012).
- [52] S. Marčelja and N. Radić, *Chem. Phys. Lett.* **42**, 129 (1976).
- [53] K. Bohinc, A. Shrestha, and S. May, *Eur. Phys. J. E: Soft Matter Biol. Phys.* **34**, 108 (2011).
- [54] D. L. Z. Caetano, G. V. Bossa, V. M. de Oliveira, M. A. Brown, S. J. de Carvalho, and S. May, *Phys. Chem. Chem. Phys.* **18**, 27796 (2016).
- [55] D. Pettifor and M. Ward, *Solid State Commun.* **49**, 291 (1984).
- [56] P. K. Shukla and B. Eliasson, *Phys. Rev. Lett.* **108**, 165007 (2012).
- [57] L. G. Stanton and M. S. Murillo, *Phys. Rev. E* **91**, 033104 (2015).
- [58] M. A. Brown, G. V. Bossa, and S. May, *Langmuir* **31**, 11477 (2015).
- [59] D. L. Caetano, G. V. Bossa, V. M. de Oliveira, M. A. Brown, S. J. de Carvalho, and S. May, *Phys. Chem. Chem. Phys.* **19**, 23971 (2017).
- [60] G. V. Bossa, D. L. Z. Caetano, S. J. de Carvalho, and S. May, *Electrochim. Acta* **321**, 134655 (2019).
- [61] M. V. Fedorov and A. A. Kornyshev, *Chem. Rev.* **114**, 2978 (2014).
- [62] J. N. Israelachvili, S. J. Kott, M. L. Gee, and T. A. Witten, *Macromolecules* **22**, 4247 (1989).
- [63] L. Lu and M. L. Berkowitz, *J. Chem. Phys.* **124**, 101101 (2006).
- [64] N. Choudhury and B. M. Pettitt, *J. Am. Chem. Soc.* **127**, 3556 (2005).
- [65] J. J. Howard, J. S. Perkyns, N. Choudhury, and B. M. Pettitt, *J. Chem. Theory Comput.* **4**, 1928 (2008).